metals

MDPI

Article

Influence of Pr^{3+} and CO_3^{2-} Ions Coupled Substitution on Structural, Optical and Antibacterial Properties of Fluorapatite Nanopowders Obtained by Precipitation

Dušan V. Milojkov [1,*], Miroslav Sokić [1], Ana Radosavljević-Mihajlović [1], Vojislav Dj. Stanić [2], Vaso Manojlović [3], Dragosav R. Mutavdžić [4] and Marija Milanović [5]

1 Institute for Technology of Nuclear and Other Mineral Raw Materials, Franchet d'Esperey 86, P.O. Box 390, 11000 Belgrade, Serbia; m.sokic@itnms.ac.rs (M.S.); a.radosavljevic@itnms.ac.rs (A.R.-M.)
2 Vinča Institute of Nuclear Sciences, University of Belgrade, P.O. Box 522, 11001 Belgrade, Serbia; voyo@vin.bg.ac.rs
3 Faculty of Technology and Metallurgy, University of Belgrade, Karnegijeva 4, 11120 Belgrade, Serbia; v.manojlovic@tmf.bg.ac.rs
4 Institute for Multidisciplinary Research, University of Belgrade, Kneza Višeslava 1, 11030 Belgrade, Serbia; gane@imsi.bg.ac.rs
5 Department of Materials Engineering, Faculty of Technology Novi Sad, University of Novi Sad, Bulevar Cara Lazara 1, 21000 Novi Sad, Serbia; majam@uns.ac.rs
* Correspondence: d.milojkov@itnms.ac.rs; Tel.: +381-11-3691-722

Citation: Milojkov, D.V.; Sokić, M.; Radosavljević-Mihajlović, A.; Stanić, V.D.; Manojlović, V.; Mutavdžić, D.R.; Milanović, M. Influence of Pr^{3+} and CO_3^{2-} Ions Coupled Substitution on Structural, Optical and Antibacterial Properties of Fluorapatite Nanopowders Obtained by Precipitation. *Metals* **2021**, *11*, 1384. https://doi.org/10.3390/met11091384

Academic Editors: Alexander Tsouknidas and Frank Czerwinski

Received: 23 July 2021
Accepted: 29 August 2021
Published: 31 August 2021

Abstract: Coupled substitution of fluorapatite (FAP) crystal lattice plays an important role in the engineering of optically active nanomaterials. Uniform fluorapatite nanopowders doped with praseodymium (Pr^{3+}) and carbonate (CO_3^{2-}) ions have been successfully synthesized by precipitation method under room temperature (25 °C). The structural, morphological, chemical and optical properties of monophase material were characterized by X-ray diffraction (XRD), Fourier Transform Infrared and Far Infrared Spectroscopy (FTIR and FIR, respectively), Scanning Electron Microscopy with Energy Dispersive Spectroscopy (SEM/EDS), Transmission Electron Microscopy (TEM) and Photoluminescence Spectroscopy (PL). Coupled substitution of FAP crystal lattice with Pr^{3+} and CO_3^{2-} reduces the crystallite size with a constant c/a ratio of 1.72. FTIR study showed that synthesized nanopowders were AB-type CO_3^{2-} substitution, and FIR study revealed new Pr–O vibrations. TEM analysis was found that synthesized nanopowders were composed of irregular spheres in the nanometer range. The fluorescence of FAP nanoparticles was in the violet-blue region of the visible part of the spectrum. When Pr^{3+} was doped in a lattice, the violet-blue emission becomes sharper due to reabsorption. MCR–ALS analyses of fluorescence spectra indicated the shift of the maximum to the blue color with the increase in the concentration of Pr^{3+} ions. Additionally, luminescent nanopowders demonstrated significant antibacterial activity against *Escherichia coli*. As the obtained nanoparticles showed a good absorption of ultraviolet A light and reabsorption of blue-green luminescence, they are suitable for further development of optically active nanomaterials for light filtering. Optically active PrCFAP nanopowders with antibacterial properties may be promising additives for the development of multifunctional cosmetic and health care products.

Keywords: fluorapatite nanopowder; optically active nanomaterials; coupled substitution; Pr^{3+}; CO_3^{2-}; antibacterial activity

1. Introduction

A wide range of multifunctional nanomaterials for biomedical use has been synthesized using different ionic substitutions in the fluorapatite (FAP) crystal lattice [1–4]. FAP has the formula $Ca_{10}(PO_4)_6F_2$ per unit cell and can be commonly found in nature as geological material and biomaterial in calcified tissue [4,5]. One of the main characteristics of FAP crystals is their structural capacity to accept many ionic substitutions [6]. A common

occurrence in apatite is the so-called coupled substitution [6]. In this substitution, one ion is replaced by another with the same sign but with a different charge; the neutrality is preserved by replacing the ions of the opposite charge or by forming vacancies. The addition of various dopants in FAP has attracted increasing attention in the last few decades for developing suitable luminescent materials for various application areas such as bone and teeth tissue reparation, bioimaging contrast agents, antimicrobial nanomaterials, as well as photoactive catalysts [7–11].

FAP nanocrystals are potentially important hosts for optically active trivalent rare-earth (RE^{3+}, or lanthanide) ions due to the unusually high crystal field splitting which supports large transition cross sections of dopant atoms [12]. FAP as a host material provides a crystal lattice with a hexagonal symmetry space group *P63/m*, which can fit the dopant lanthanides ions at two different Ca structural positions (Ca1 (*4f*) and Ca2 (*6h*) sites) [2]. Lanthanides ions such as Ce^{3+}, Pr^{3+}, Nd^{3+}, Sm^{3+}, Eu^{3+}, Tb^{3+}, Dy^{3+}, Er^{3+}, Tm^{3+} and Yb^{3+} can be commonly doped in apatite crystal lattice [12]. The unique optical properties of lanthanide ions originate from electronic transitions within the 4*f* shell or from the 4*f* to 5*d* shell, so that these fluorophores absorb light of a certain wavelength and re-emit a quantum of light with energy proportional to the energy difference between the excited state and the ground state [13]. In addition to these luminescent properties, doped RE^{3+} ions also lead to some changes in the physico-chemical and biological properties of FAP nanoparticles [13]. Pr^{3+} ion, a well-known activator dopant, posesses unique optical properties, along with the tunable emission wavelengths ranging from ultraviolet (UV) to infrared (IR) region [14]. Some authors think that in general Pr^{3+} is probably more important as a sensitizer of other RE^{3+} than for its own emission [15]. Furthermore, when Pr^{3+} was implanted into TiN coatings, it effectively improved corrosion resistance and hemocompatibility of this biomedical implant [16]. In addition, praseodymium can act as a good antibacterial and mild antifungal agent [17]. Due to the increasing resistance of bacteria to antibiotics, FAP nanomaterials doped with metals have attracted a lot of attention as a possible new type of antibacterial agent [9]. Antimicrobial agents are highly relevant for various industrial applications in environmental, food, synthetic textiles, packaging, health care and medical care products [9].

All substitutions of FAP crystal structure exist in nature and most of them can be reproduced in laboratory conditions [6]. According to the literature, luminescent RE^{3+}-doped FAP materials were synthesized using high-temperature methods [18], hydrothermal methods under temperature and pressure [19] or precipitation methods that follow high-temperature calcination [8]. In a previous study of Milojkov et al. [8], nanocrystals of Pr^{3+} doped FAP were precipitated under mild conditions, followed by calcination at 700 °C. In this study, poorly crystallized nanopowders of FAP co-doped with Pr^{3+} and CO_3^{2-} were synthesized by the precipitation, the first step of the method described in [8], and obtained nanopowders were characterized according to crystallinity, morphology and chemical content. Chemical precipitation is based on the fact that fluorapatite is at least soluble at room temperature and in the base medium (pH 10) and is usually the most stable phase of calcium phosphate in an aqueous solution [20]. According to literature data, many synthesis parameters, such as reactant concentration, temperature, pH and aging time, influence the properties of the obtained fluorapatite precipitate [19–21]. This paper will show the phenomena of the coupled substitution of FAP crystal lattice, which occurs when Pr^{3+} reaches the Ca^{2+} site, and the excess of positive charge is compensated by incorporating CO_3^{2-} from solution or air. Photoluminescence excitation and emission of samples were evaluated to explore the optical performance of Pr^{3+}- and CO_3^{2-}-doped FAP, and the resulting spectra were statistically analyzed. Antibacterial activity against *Escherichia coli* (*E. coli*) was tested to define these inorganic luminescent nanoparticles as antimicrobial materials for health care and cosmetics applications.

2. Materials and Methods

2.1. Preparation of Nanopowders Samples

The starting material is prepared by precipitation method at room temperature (25 °C). The following starting chemicals were used to synthesize powders: $Ca(NO_3)_2 \cdot 4H_2O$ (Merck, min. 98.5%), $(NH_4)_2HPO_4$ (Merck, 99%), $(NH_4)F$ (VWRBDH Prolabo, min. 96%) and $Pr(NO_3)_3 \cdot 6H_2O$ (REACHIM, chemically pure). Double distilled water was used throughout all the experiments. Four precipitates were produced with a constant ratio of (Pr + Ca)/P at 1.67. These compositions correspond to 0.1%, 0.5% and 1% Pr^{3+} substitution for Ca^{2+}. The required amount of $(NH_4)_2HPO_4$ and $(NH_4)F$ was dissolved in 200 mL water and added dropwise to the solution containing the required amount of $Ca(NO_3)_2 \cdot 4H_2O$ and $Pr(NO_3)_3 \cdot 6H_2O$ in 200 mL, with continuous mechanical stirring (500 rpm). After solution adding, pH is adjusted to the same level (pH = 10 $\pm$ 0.5) by adding NH_4OH, and the suspension was maturated for 16 h at room temperature. The obtained precipitate is filtered and washed with deionized water and afterward dried at 110 °C for 12 h. The resulting amorphous materials were pulverized into powder and characterized. The samples were noted down as FAP and Pr*x*CFAP, where *x* stands for the atomic percentage of Pr^{3+} ions (x = 0.1, 0.5, 1.0%).

2.2. Characterization of Nanopowders

X-ray powder patterns were recorded on an X-ray powder diffractometer Rigaku Ultima IV (Rigaku Americas Corporation, Tokyo, Japan), using nickel-filtered $CuK\alpha_{1,2}$ radiation (λ = 0.1540 nm, operating at 40 kV and 40 mA). XRD data were collected from 4° to 80° (2θ) at a scanning rate of 0.02°/s. JCPDS-ICDD database (File Card no. 83-0557. Washington, DC, USA) and software program Diffrac. Eva (version 1., Bruker, Karlsruhe, Germany) were used for identification. For the processing of the X-ray powder diagram, the program Powder Cell (version 2.4., Federal Inst. Materials Res. and Testing (BAM), Berlin, Germany) was used [22].

Fourier Transform Infrared Spectra (FTIR) were recorded in the range of 4000 to 400 cm^{-1} using Nicolet 6700 FTIR spectrophotometer (Thermo Fisher Scientific, Waltham, MA, USA) and the ATR technique. The same spectrophotometer was used to record Far Infrared (FIR) Spectra in the range of 400 to 100 cm^{-1}.

Scanning electron microscopy (SEM) analyses were obtained by scanning electron microscope (SEM, JEOL JSM–6390LV, Peabody, MD, USA) at room temperature with 30 kV acceleration voltage in a nitrogen atmosphere. The chemical composition of the samples was obtained by energy dispersive spectroscopy (EDS, Oxford Aztec X-max, Abingdon, UK). Transmission electron microscopy (TEM) was performed using FEI Talos F200X microscope (Thermo Fisher Scientific, Waltham, MA, USA), operated at 200 keV.

2.3. Photoluminescent Study and Fluorescence Data Analysis

Photoluminescence spectrophotometer Horiba JovinYvon Fluoromax 4 TCSPC (Jobin Yvon Horiba, Paris, France) was used to record the emission and excitation spectra of the samples. A Xenon lamp of 450 W was used for all excitations. All measurements were performed at room temperature from the prepared nanopowders after synthesis. As in the case of coupled substitutions of FAP nanomaterials, it is a multicomponent system, and additional fluorescence of the samples was measured in the wavelength range of 350 to 600 nm and statistically analyzed. For each nanopowder, a series of emission spectra were collected by excitation at different wavelengths in the range of 320 to 350 nm with a 3 nm step. The spectra were obtained with an integration time of 0.1 s and 1 nm slits for excitation and emission. In this way, an excitation–emission matrix with dimension 11 $\times$ 251 is formed for each sample, which was analyzed by using the Multivariate Curve Resolution–Alternating Least Squares (MCR-ALS) method. MCR-ALS is a chemometric method that is successfully used to extract relevant information about pure components in multicomponent systems using bilinear decomposition of the experimental matrix. All anal-

yses were performed by using the unscramble software package (The Unscrambler × 10.4, Camo ASA, Trondheim, Norway).

2.4. Antibacterial Activity Test of Obtained Nanopowders

According to the liquid challenge method, the antibacterial activity test of all the obtained powders against *E. coli* (ATCC 25922) was performed in a phosphate buffer solution [13,14]. Culture medium LAB 8 nutrition agar (Lab M, Bury, United Kingdom) was used to test bacteria growing. Phosphate buffer solution (0.133 M, pH 7.2) was made by dissolving KH_2PO_4 and Na_2CO_3 (p.a. grade, Merck, Darmstadt, Germany) in deionized water.

The strains were cultivated on agar slants at 37 °C in a thermostat for 24 h. Initial bacterial inoculums were obtained by cell dispersion from the surface of well-grown bacterial slant culture in 3.0 mL of the sterile buffer thermostated at 37 °C. The 9.9 mL of sterile phosphate buffer solution was inoculated with 0.1 mL of a microorganism's inoculum. A mass of 100 mg of investigated fluorapatite sample (sterilized in the tube at 180 °C for two hours to avoid microorganism impurities) was challenged to 10 mL of the bacterial suspension. After 0.5, 1 and 2 h of incubations, 1 mL aliquots were taken as samples for viable cell determination. One-hundred microliters of appropriate dilution was placed in Petri dish and overlaid with TSAY (Tripton soy agar with 0.6% yeast extract) and thermostating for 24 h. As controls, the buffer was also challenged to chosen strains without investigated sample. The degree of microorganism reduction (R (%)) was calculated using the following Equation (1):

$$R\ (\%) = 100 \times (C_0 - C)/C_0 \quad (1)$$

where C_0 is the average number of the strain colonies of the control and C is the corresponding number of strain colonies of challenged samples at the same predetermined time. All analyses of antibacterial activity determination were run in triplicate, and average values with deviation were taken as the results.

3. Results and Discussion

3.1. Characterization of Synthesized Nanopowders

Synthesized nanostructures were subjected to XRD analysis to determine the structure, composition and phase purity. The XRD patterns of FAP and Pr*x*CFAP samples are presented in Figure 1. Intensities and positions of all diffraction peaks are consistent with corresponding standard patterns of the FAP phase [JCPDS 83–0557] (space group *P63/m*), and no additional crystalline phases could be detected. Broad peaks and small intensities indicate a small crystallite size and a low degree of crystallinity. The patterns of the synthesized pure FAP and Pr^{3+}-doped Pr*x*CFAP samples are similar, indicating that Pr^{3+} has been successfully substituted into the crystal lattice of FAP.

To investigate the influence of the addition of Pr^{3+} in the FAP crystallite, the lattice parameters are compared and presented in Table 1. Lattice parameters *a* and *c*, and unit cell volume decrease for all samples when dopant concentration increases, except for the sample Pr0.1CFAP. These shrinks are small and they are the result of the replacement of larger ion with smaller, due to the difference in radius between Pr^{3+} (1.12 Å) and Ca^{2+} (1.13 Å) ions [23]. Furthermore, crystallite size decreases with an increase of dopant ions concentration for all samples. Crystallite sizes calculated by Scherrer's formula are d (FAP) = 20 nm, d (Pr0.1CFAP) = 21 nm, d (Pr0.5CFAP) = 19 nm and d (Pr1CFAP) = 15 nm. This decrease of apatite crystallite size with increasing of RE^{3+} ions substitutions agrees with previous reports of substitution of Eu^{3+} and Ce^{3+} in FAP lattice [24,25]. As rare-earth ions are similar in radius to Ca^{2+} ions, in natural apatites, they replace both positions in the lattice (Ca1 and Ca2) [26]. There was also a possibility that Pr^{3+} ions did not substitute Ca^{2+} positions exclusively when dopant ion appears in special positions in the crystal structure which modifies the crystal environment [6]. This might be a reason for the small increase of parameters in the sample Pr0.1CFAP. The ratio of the lattice parameters *c*/*a* for

all samples is 0.73. This constant ratio of parameters confirms that the hexagonal apatite structure is not disturbed by the substitution of Pr^{3+} ions. Small variations in the crystal lattice parameters indicate that there are certain deformations in the crystal structure.

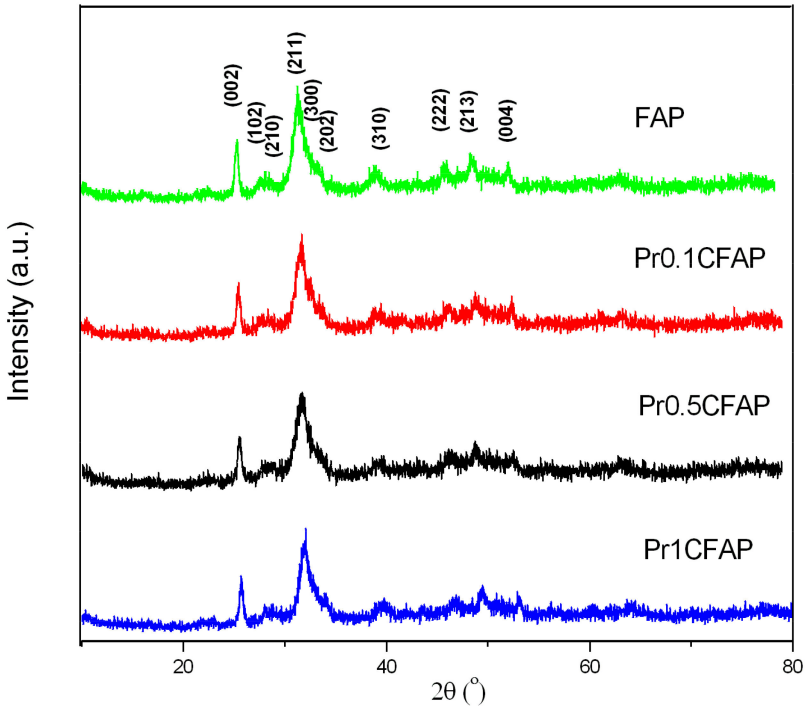

Figure 1. XRD patterns of the FAP and Pr*x*CFAP samples.

Table 1. Unit cell parameters, crystallite size and strain of FAP and PrxCFAP samples.

Sample	Unit Cell Parameters			Crystallite Size	Strain
	a (Å)	c (Å)	V (Å^3)	(nm)	
FAP	9.328 (4)	6.837 (4)	515.213	20	0.007328
Pr0.1CFAP	9.339 (4)	6.825 (4)	515.602	21	0.007524
Pr0.5CFAP	9.317 (4)	6.825 (4)	513.072	19	0.007999
Pr1CFAP	9.305 (4)	6.813 (4)	510.905	15	0.008162

The fluorapatite material crystallizes in the hexagonal *P*63/m (No. 176) space group with ten Ca^{2+} ions placed in two different crystallographic symmetry positions: Ca1(*4f*) and Ca2 (*6h*). Both cationic sites are available for substitution with rare-earth (RE^{3+}) ions, involving a charge compensation mechanism when substituting the divalent calcium cation by a trivalent praseodymium cation [12]. Pr^{3+} has very similar ionic radii with Ca^{2+}, but more of the electronic charge of the cloud, so that fluorapatite doped with Pr^{3+} may exhibit different site distribution characteristics instead of Ca^{2+}. Earlier studies regarding site preference of rare earth elements in fluorapatite have shown that Pr^{3+} had substituted Ca^{2+} in Ca2 sites [8,26].

FTIR spectra of the FAP and Pr*x*CFAP samples are shown in Figure 2. The FTIR spectra of each of the samples contain characteristic bands of apatite compounds (Table 2).

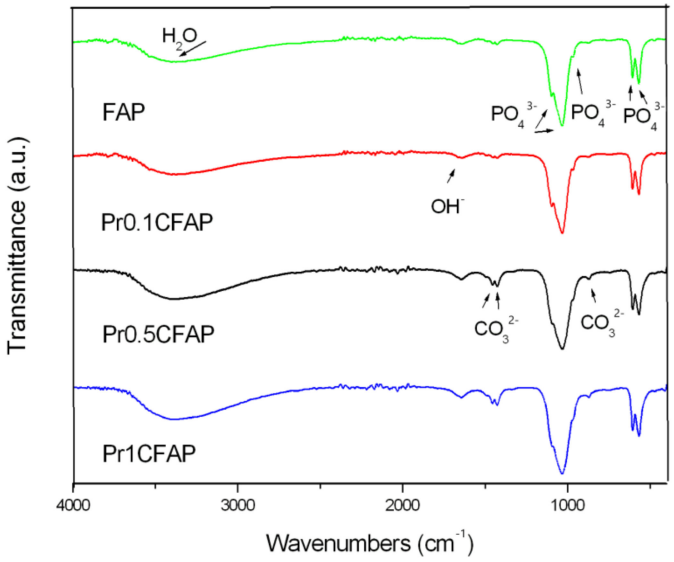

Figure 2. FTIR transmittance spectra of the FAP and Pr*x*CFAP samples.

Table 2. FTIR vibration bands for FAP and PrxCFAP samples.

Sample	Vibration Bands (cm^{-1})							
	PO_4^{3-} (ν_4)		CO_3^{2-}	PO_4^{3-} (ν_1)	PO_4^{3-} (ν_3)		CO_3^{2-}	OH^-
FAP	565.4	603.8		966.4	1032.1	1095.7	1427.3	1643.7
Pr0.1CFAP	566.0	604.4		966.8	1032.1	1095.8	1427.4	1637
Pr0.5CFAP	565.6	603.9	866.6	966.3	1031.8	1094.4	1428.6	1636.2
Pr1CFAP	565.2	603.5	864	964.3	1031.3	1094.1	1427.1–1455.1	1646.2

The bands that appear at 565–603 cm^{-1} belong to the (ν_4) stretching symmetric vibrations of PO_4^{3-} groups, while the bands at 1032–1095 cm^{-1} originate from asymmetric stretch vibration (ν_3). When dopant concentration increases in samples, the small band appears at about 866, 1427 and 1456 cm^{-1} (for the ν_3 band) which is ascribed to CO_3^{2-} ions [27,28]. Bands at 866, 1427 and 1456 cm^{-1} indicated AB-type substitution of PO_4^{3-} and F^- ions with CO_3^{2-} [29]. When the synthesis of fluorapatite is performed from an aqueous solution under moderate conditions in an open system, the incorporation of CO_2 from the atmosphere is favored [30]. These ions appear because divalent calcium cations were substituted by trivalent praseodymium cations due to charge compensation. Some researchers do not assign the bands at 880, 1420 and 1450 cm^{-1} to the carbonated apatite, because they may originate from the carbonate adsorbed on the surface of apatite crystals or separated carbonate phase with apatite crystals [31]. These negatively charged ions adsorbed on the surface can be removed if the resulting precipitate was washed with ethanol [32]. A small peak at about 1650 cm^{-1} belongs to the vibrations of the OH^- groups. During the synthesis of FAP from an aqueous solution, a small amount of F^- ions will always be replaced by OH^- ions [9]. The broadband at 2500–3700 cm^{-1} and a small band at about 1650 cm^{-1} were associated with water absorbed and present in the dried samples.

FIR transmittance spectra in the range of 200 to 600 cm^{-1}, shown in Figure 3, correspond with bending vibration of P-O bonds phosphate group coupled with the vibrations of contacts between metal and oxygen M-O and O-M-O (Table 3).

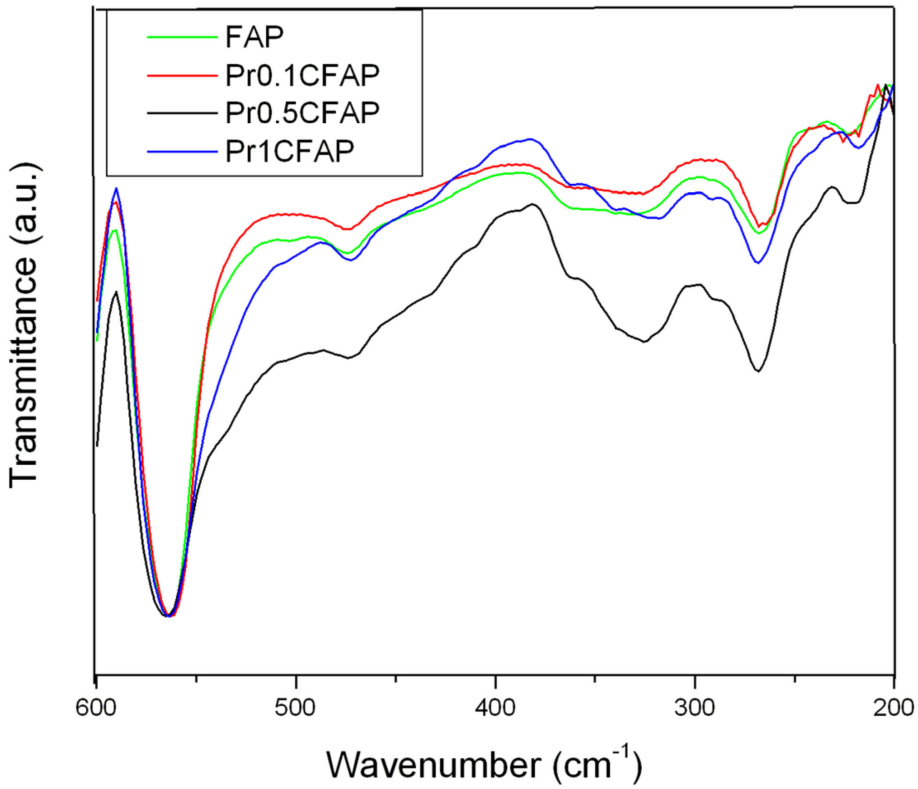

Figure 3. FIR transmittance spectra of FAP and Pr*x*CFAP samples.

Table 3. FIR vibration bands for FAP and Pr*x*CFAP samples.

Sample	Vibration Bands (cm^{-1})						
	PO_4^{3-} (ν_4)	PO_4^{3-} (ν_2)	Pr-O		O-M-O (d_m)	O-M-O (d_w)	M-O (ν_w)
FAP	565.4	477.6			331.4	267.9	223.1
Pr0.1CFAP	562.8	474.1			326.0	267.7	225.6
Pr0.5CFAP	565.1	473.5	400.1	360.6	325.6	268.4	221.6
Pr1CFAP	563.8	673.1	400	360 340.2	318.5	268.5	218.1

These FIR frequencies are primarily dependent on the M-O bonds and will vary as the cation changes. Samples of pure FAP and Pr0.1CFAP have a similar distribution of peaks. Namely, there is a pronounced band of P-O vibration at 560 cm^{-1} and 470 cm^{-1}, and three weaker bands at 470, 280 and 220 cm^{-1} coupled with scissoring deformation vibration in the plane O-M-O (δ_m) at 331 cm^{-1}, wagging deformation vibration in the plane O-M-O (δ_w) at 267 cm^{-1} and bending deformation vibration out of plane M-O (ν_w) at 223 cm^{-1} (Table 3) [33]. In samples Pr0.5CFAP and Pr1CFAP, these three bands are also present, and in addition, there is also a new band in the range of 400 to 320 cm^{-1}, which comes from the added Pr^{3+} ions. The absorption intensities of the bands increase with increasing dopant concentration, for the samples Pr0.5CFAP and Pr1CFAP, because the intensity of the bands depends on the magnitude of the change in the dipole moment.

Morphology along with the elemental composition of FAP and Pr*x*CFAP samples is shown in Figure 4.

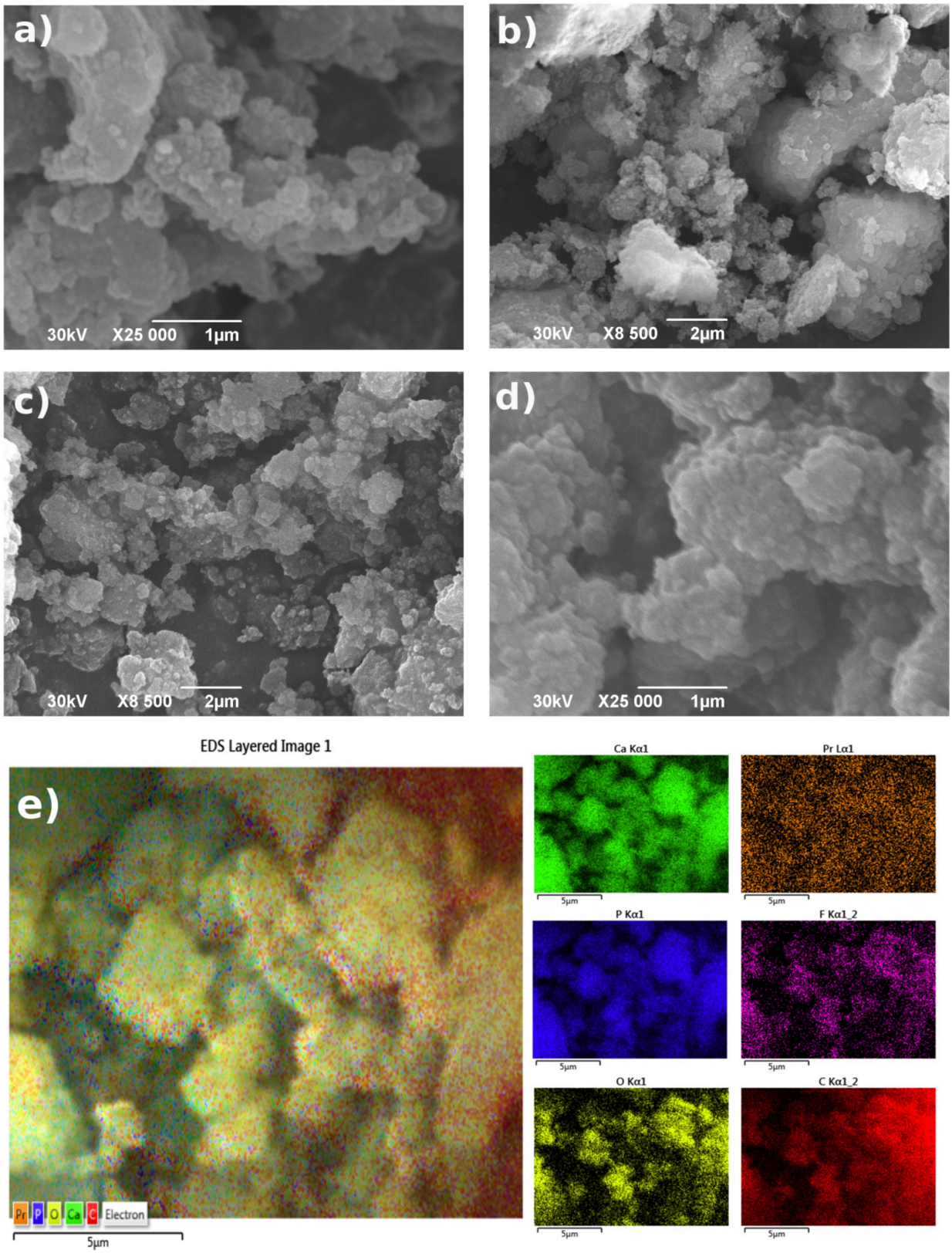

Figure 4. Scanning electron micrographs of FAP (**a**), Pr0.1CFAP (**b**), Pr0.5CFAP (**c**) and Pr1CFAP (**d**) samples. EDS mapping distribution of elements in the Pr1CFAP sample (**e**).

The SEM images (Figure 4a–d) show that FAP and Pr*x*CFAP samples are composed of nanosized particles with irregular sphere-like shape which easily form agglomerates. The higher magnification obtained by TEM analyses confirmed that nanoparticles are spherical

and highly agglomerated (see Figure 5). The prepared fluorapatite nanomaterials have an average size of particles of about 20 nm; this is consistent with the crystallite size results calculated from the XRD data analysis. Figure 4e shows the EDS mapping with the spatial distribution of elements in a sample of Pr^{3+} doped FAP with the highest concentration. The EDS spectra of the powders confirmed the presence of all constituent elements of Pr1CFAP powders. It can be seen that Pr^{3+} ions are distributed uniformly per sample instead of Ca^{2+}.

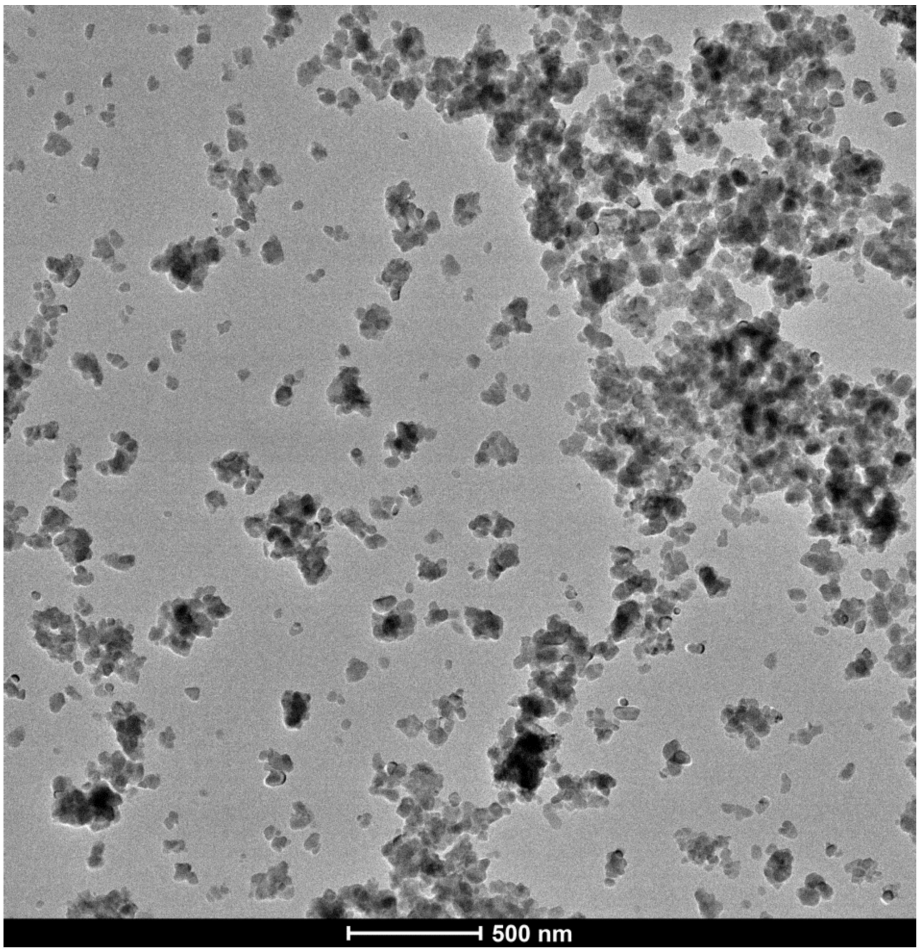

Figure 5. TEM image of the Pr0.5CFAP nanopowder.

3.2. Photoluminescence Properties of Obtained Nanopowders

The photoluminescence excitation spectra measured for all samples at room temperature are depicted in Figure 6a. All samples have an excitation maximum at about 350 nm, originated from the charge transfer (CT) bands F^{-}–Ca^{2+} of the host lattice. After praseodymium was added to the FAP lattice, the compounds still exhibited a strong broad host absorption band with increasing absorption intensity. The position of the O^{2-}–Pr^{3+} charge transfer absorption band is assumed to be situated at 285 nm. Typical Pr^{3+} *f–f* transition bands are not visible in the longer wavelength region because of their significantly lower emission intensity in comparison to that of the FAP host excitation band. It proves the high efficiency of the energy transfer (ET) between the host matrix and the dopant ions.

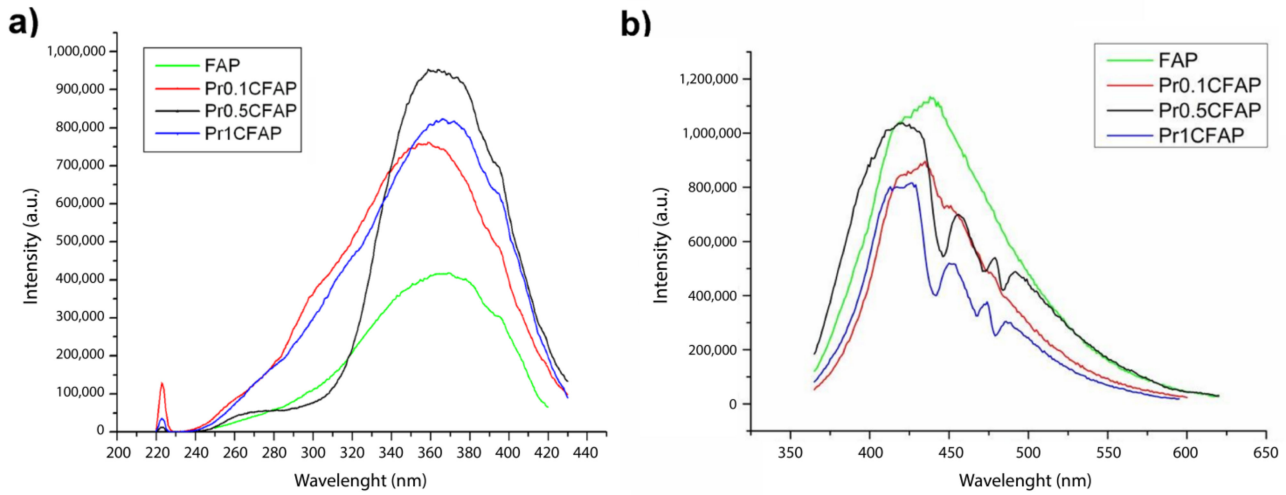

Figure 6. (**a**) Excitation (for emission max. at 435 nm) (**b**) and emission spectra (under excitation of 350 nm) of FAP and PrxCFAP samples obtained at room temperature.

Emission spectra of FAP and PrxCFAP samples obtained at excitation of 350 nm are shown in Figure 6b.

The pure FAP sample exhibited a strong broad host emission band in the violet-blue region of the visible part of the spectrum. After praseodymium was added to the FAP lattice, the compounds still exhibited a strong broad host emission band with additional re-absorption transitions of the Pr^{3+} ion. Furthermore, note that the broad host emission band becomes sharper with an increasing concentration of Pr^{3+}. The additional absorption peaks between 440 and 500 nm are assigned to the typical $4f^2$–$4f^2$ intra-configuration forbidden transitions of Pr^{3+}. These reabsorption peaks in the emission spectra at 448, 473 and 487 nm correspond to $^3H_4$–$^3P_2$, $^3H_4$–$^3P_1$, $^1I_6$ and $^3H_4$–$^3P_0$ transitions, respectively [34]. It can be noticed missing of the peak at 595 nm associated with the ground $^3H_4$ level and the excited $^1D_2$ level which was characteristic for FAP microcrystal doped with Pr^{3+}, and nanocrystal as well [8,18,34]. This is due to the presence of anionic species that quenching luminescence and high energy transfer efficiencies between the nano-FAP host matrix and the dopant ion. The luminescence quenching from $^3P_0$ levels in carbonate-fluorapatite has been described by previous research as a consequence of the transfer of excitation energy to the lattice vibrations [35]. For rare earths, significant quenching occurs when the difference in energies between electronic levels is approximately equal to the energy of four phonons [35,36]. The energy difference between the $^3P_0$ lower $^1D_2$ level is approximately 3580 cm^{-1}, which is particularly equivalent to the four phonons of ν_2 vibration of the carbonate groups (870–880 cm^{-1}) (see Table 2) [35,36]. It can be concluded that the emission of Pr^{3+} at the FAP matrix is dependent on defects in material and unintentional impurities, which modify emission spectra.

The Multivariate Curve Resolution–Alternating Least Squares method (MCR–ALS) was used for spectral decomposition of the excitation–emission matrix into signals of individual components (Figure 7). Three-component analysis was adequate for all samples, except for the Pr1CFAP sample. The left side of Figure 7 shows a three-component analysis of the samples. The obtained values for the emission component maximums are listed in Table 4. MCR–ALS analysis shows that position of a first component K1 (blue lines at right plots in Figure 7) is slightly lower for the samples FAP and Pr0.5CFAP, but red shift occurs from FAP to Pr1CFAP. Component K2 (red lines at right plots in Figure 7) also shows red shift going from FAP to Pr0.1CFAP and Pr1CFAP samples, while the Pr0.5CFAP sample slightly deviates from this trend. Component K3 (green lines at right plots in Figure 7) shows a blue shift going from FAP to Pr0.1CFAP and Pr0.5CFAP samples. For Pr1CFAP sample component K3 merges with the component K2 and extinguishes, leading to the creation of vacancies in the structure. Further, obtained values for the emission component

maximums listed in Table 4. indicate the shift of the maximum to the blue color and the quenching of the UV component with the increase in the concentration of Pr^{3+} ions.

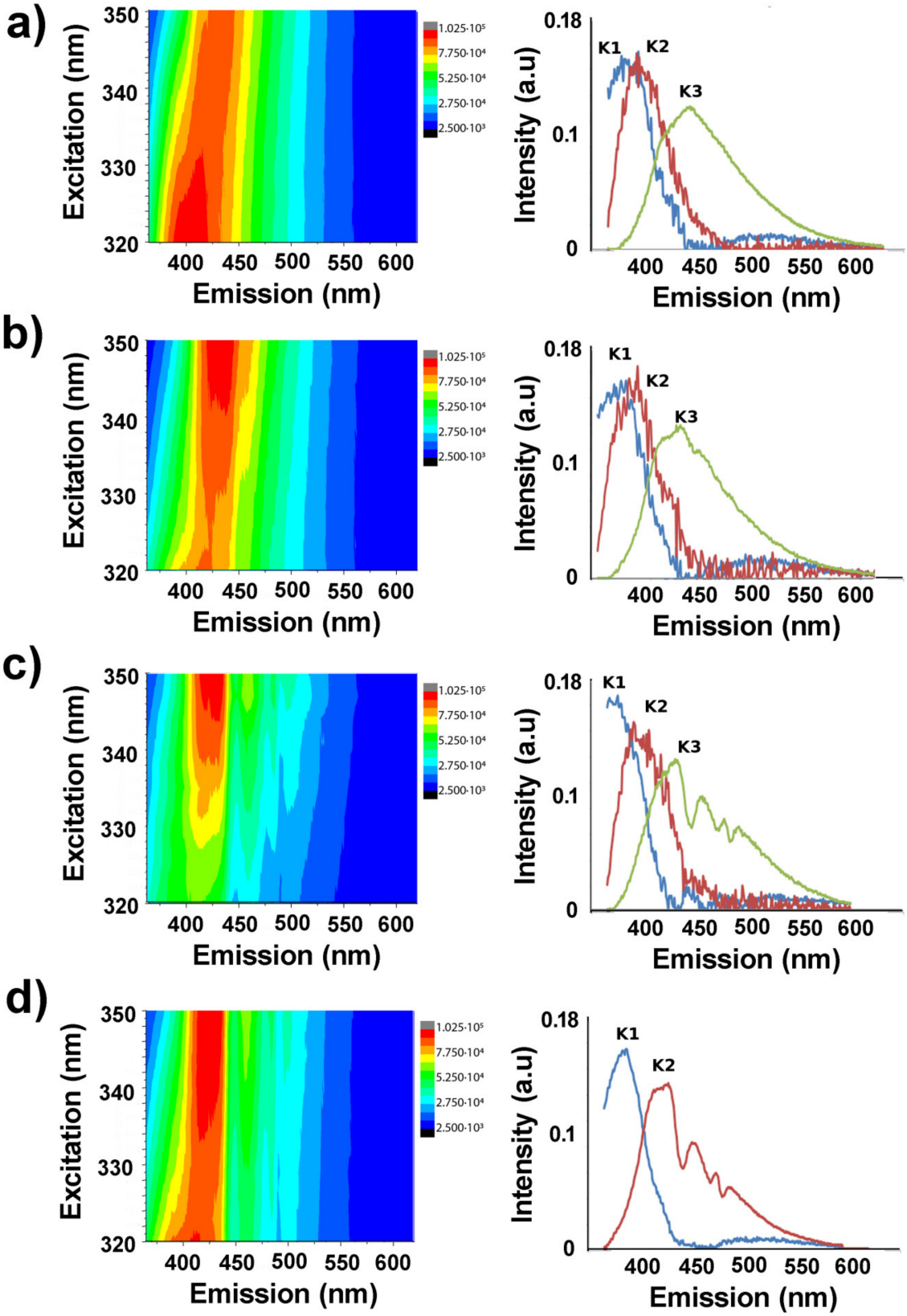

Figure 7. Excitation–emission maps (**left**), and emission components (K1, K2 and K3) obtained by applying the MCR–ALS method analysis (**right**) of FAP (**a**), Pr0.1CFAP (**b**), Pr0.5CFAP (**c**) and Pr1CFAP (**d**) samples.

Table 4. Values of three-component analysis of the samples.

Sample	Component Maximus (nm)		
	K1	K2	K3
FAP	377	388	435
Pr0.1CFAP	384	397	434
Pr0.5CFAP	372	396	430
Pr1CFAP	384	423	-

The analysis of emission spectra together with the results of XRD and FTIR analysis leads to the conclusion that there is a replacement of Ca^{2+} with Pr^{3+} ions in the system, which is accompanied by charge compensation in the form of incorporation of CO_3^{2-} and HO^- anionic species that quenching dopant luminescence.

In general, the luminescent properties of doped FAP nanoparticles, but also the ultimate functional characteristics, essentially depend on the crystallinity, the concentration of activator ions, as well as on the stoichiometry of the compound, and the possible presence of other ionic species.

The absence of additional emission transitions of Pr^{3+} ions is a consequence of impurities in the crystal lattice in the form of CO_3^{2-} and OH^- ions and residual water. CO_3^{2-} ions and H_2O molecules increase the phonon energy of the crystal lattice and retain energy transitions in Pr^{3+} ions. Moreover, an increase in the concentration of OH^- ions in the crystal lattice can lead to a decrease in the luminescence intensity of Pr^{3+} ions. If OH^- ions are on the surface of the crystal, then they will also behave as excitation acceptors, so that they can completely extinguish luminescence. Complete quenching of the luminescence in the doped FAP system occurs due to the existence of a center for capturing excitation on the particle surface (OH^- acceptors) or due to the disturbed symmetry of the luminescence center in the crystal lattice of the FAP [37].

3.3. Determination of the Antibacterial Activity of Obtained Nanopowders

E. coli species are involved in various skin and soft tissue infections [38]. In recent years, there has been a dramatic drop in the sensitivity of pathogenic strains of *E. coli* to antibiotics, so there is a need to develop new and innovative antibacterial agents [38]. The antibacterial activity of FAP and PrxCFAP samples against *E. coli* bacteria was studied after 0.5, 1 and 2 h incubation and results are presented in Figure 8.

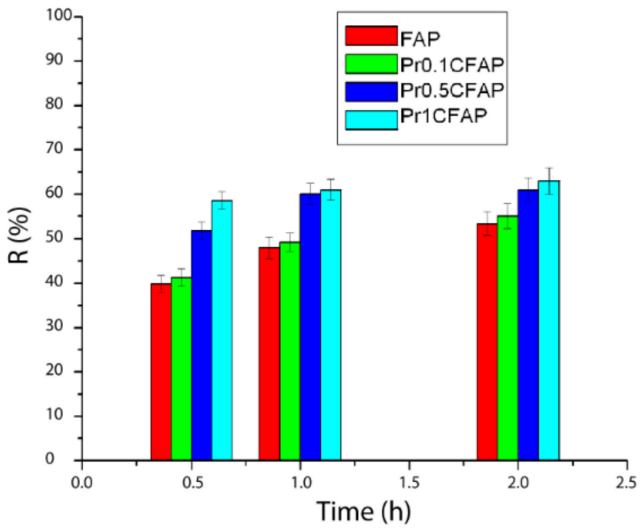

Figure 8. The percentage of bacterial reduction (R%) for *E. coli* after the treatment with the synthesized powders in time.

The FAP sample showed antibacterial activity against tested *E. coli* strain, and the degree of reduction was about 50% after 2 h of exposure (Figure 8). The reduction can be associated with the interaction of bacterial cells and surfaces of FAP particles as well as with released fluoride ions. According to the previous studies, FAP materials show antibacterial activity but not biocide effect [9,20]. Pr0.1CFAP sample showed more than 55% of reduction after 2 h, while samples Pr0.5CFAP and Pr1CFAP exerted a little bit higher degree of reduction, i.e., 65% after 1 and 2 h, respectively (Figure 8). This higher reduction ratio of doped samples can be associated with increasing Pr^{3+} and CO_3^{2-} ions concentration and consequently to its higher release from the crystal structure. Finally, decreasing the nanopowder's crystals size causes a higher degree of bacterial reduction ratio. Previous studies have shown that use of fluoride either alone or in combination with other antibacterial agents has proved to be effective in reducing the growth of bacteria [9,20]. Optically active Pr*x*CFAP nanopowders with antibacterial properties may be promising additives for the development of multifunctional cosmetic and health care products.

4. Conclusions

The precipitation method has been successfully used to synthesize monophase Pr^{3+}- and CO_3^{2-}-doped fluorapatite nanoparticles with unique optical properties. XRD, FTIR, FIR, TEM and SEM-EDS analyses showed that particles of PrxCFAP are nanosized and homogenous in composition. Photoluminescence studies show emissions from the FAP lattice in the violet-blue color of visible light, which passes into the blue color region with increasing Pr^{3+} concentration. When Pr^{3+} was doped in lattice, the violet-blue emission becomes sharper without UV component due to the effect of reabsorption. In addition, the antibacterial activity of nanopowders against *E. coli* increases with an increase of dopant concentration and decreasing of crystallite size. The multifunctional properties of these nanopowders open the possibilities for their applications in the various biomedical, cosmetic, and health care preparations.

Author Contributions: D.V.M. devised and designed the experiments in addition to analyzing all data; All authors participated in the investigation and characterization of the obtained nanomaterials; M.S., V.M., M.M. and D.V.M. participated in funding acquisition; D.V.M. surveyed literature, prepared the original paper draft, and designed figures. All authors discussed the results and commented on the manuscript. All authors have read and agreed to the published version of the manuscript.

Funding: The authors are grateful to the Ministry of Education, Science and Technological Development of the Republic of Serbia (Contract number: 451-03-9/2021-14/200023) for the financial support.

Data Availability Statement: Study did not report any data.

Acknowledgments: Special thanks to Vladimir Pavlović for SEM–EDS measurement.

Conflicts of Interest: The authors declare no conflict of interest.

References

1. Golafshan, N.; Alehosseini, M.; Ahmadi, T.; Talebi, A.; Fathi, M.; Kharaziha, M.; Orive, G.; Castilho, M.; Dolatshahi-Pirouz, A. Combinatorial fluorapatite-based scaffolds substituted with strontium, magnesium and silicon ions for mending bone defects. *Mater. Sci. Eng. C* **2021**, *120*, 11161. [CrossRef]
2. Zeng, H.; Li, X.; Sun, M.; Wu, S.; Chen, H. Synthesis of Europium-Doped Fluorapatite Nanorods and Their Biomedical Applications in Drug Delivery. *Molecules* **2017**, *22*, 753. [CrossRef]
3. Hu, X.; Zhu, J.; Li, X.; Zhang, X.; Meng, Q.; Yuan, L.; Zhang, J.; Fu, X.; Duan, X.; Chen, H.; et al. Dextran-coated fluorapatite crystals doped with Yb3+/Ho3+ for labeling and tracking chondrogenic differentiation of bone marrow mesenchymal stem cells in vitro and in vivo. *Biomaterials* **2015**, *52*, 441–451. [CrossRef]
4. Fan, Q.; Cui, X.; Guo, H.; Xu, Y.; Zhang, G.; Peng, B. Application of rare earth-doped nanoparticles in biological imaging and tumor treatment. *J. Biomater. Appl.* **2020**, *35*, 55–70. [CrossRef]
5. Anderson, C.G.; Miranda, P.J. Metallurgical Evaluation of the Hoidas Lake Rare Earth Deposit. *Metall. Mater. Eng.* **2020**, *26*, 143–162. [CrossRef]
6. Leroy, N.; Bres, E.; Jones, D.B.; Downes, S. Structure and substitutions in fluorapatite. *Eur. Cells Mater.* **2001**, *2*, 36–48. [CrossRef]

7. Kushwaha, M.; Pan, X.; Holloway, J.A.; Denry, I.L. Differentiation of human mesenchymal stem cells on niobium-doped fluorapatite glass-ceramics. *Dent. Mater.* **2012**, *28*, 252–260. [CrossRef]
8. Milojkov, D.V.; Silvestre, O.F.; Stanić, V.D.; Janjić, G.V.; Mutavdžić, D.R.; Milanović, M.; Nieder, J.B. Fabrication and characterization of luminescent Pr3+ doped fluorapatite nanocrystals as bioimaging contrast agents. *J. Lumin.* **2020**, *217*, 116757. [CrossRef]
9. Stanić, V.; Radosavljević-Mihajlović, A.S.; Živković-Radovanović, V.; Nastasijević, B.; Marinović-Cincović, M.; Marković, J.P.; Budimir, M.D. Synthesis, structural characterisation and antibacterial activity of Ag+-doped fluorapatite nanomaterials prepared by neutralization method. *Appl. Surf. Sci.* **2015**, *337*, 72–80. [CrossRef]
10. Gangu, K.K.; Maddila, S.; Maddila, S.N.; Jonnalagadda, S.B. Nanostructured samarium doped fluorapatites and their catalytic activity towards synthesis of 1, 2, 4-triazoles. *Molecules* **2016**, *21*, 1281. [CrossRef]
11. Milojkov, D.V.; Stanić, V.; Dimović, S.; Mutavdžić, D.R.; Živković-Radovanović, V.; Janjić, G.V.; Radotić, K. Effects of Ag+ ion doping on UV radiation absorption and luminescence profiles of fluorapatite nanomaterials obtained by neutralization method. *Acta Phys. Pol. A* **2019**, *136*, 86–91. [CrossRef]
12. Gaft, M.; Reisfeld, R.; Panczer, G. (Eds.) *Modern Luminescence Spectroscopy of Minerals and Materials*; Springer: Berlin/Heidelberg, Germany, 2005.
13. Perera, T.S.H.; Han, Y.; Lu, X.; Wang, X.; Dai, H.; Li, S. Rare earth doped apatite nanomaterials for biological application. *J. Nanomater.* **2015**, *2015*, 705390. [CrossRef]
14. Diego-Rucabado, A.; Candela, M.T.; Aguado, F.; González, J.; Rodríguez, F.; Valiente, R.; Cano, I. A comparative study on luminescence properties of y2o3: Pr3+ nanocrystals prepared by different synthesis methods. *Nanomaterials* **2020**, *10*, 1574. [CrossRef]
15. Waychunas, G.A. Apatite luminescence. *Rev. Mineral. Geochem.* **2002**, *48*, 701–742. [CrossRef]
16. Zhang, M.; Ma, S.; Xu, K.; Chu, P.K. Corrosion resistance of praseodymium-ion-implanted TiN coatings in blood and cytocompatibility with vascular endothelial cells. *Vacuum* **2015**, *117*, 73–80. [CrossRef]
17. Ameen, I.; Tripathi, A.K.; Mishra, R.L.; Siddiqui, A.; Tripathi, U.N. A study on enhancing the quantum yield and antimicrobial activity of Pr (III) by varying the coordination environment. *RSC Adv.* **2018**, *8*, 8412–8425. [CrossRef]
18. Sardar, D.K.; Yow, R.M.; Sayka, A. Crystal-Field Splittings and Phonon Effects on a Sharp Emission Line within a Manifold of Pr3+ in Ca5(PO4)3F Laser Host. *Phys. Status Solidi B* **2001**, *223*, 691–700. [CrossRef]
19. Li, X.; Zhu, J.; Man, Z.; Ao, Y.; Chen, H. Investigation on the structure and upconversion fluorescence of Yb 3+/Ho 3+ co-doped fluorapatite crystals for potential biomedical applications. *Sci. Rep.* **2014**, *4*, 1–7. [CrossRef]
20. Stanić, V.; Dimitrijević, S.; Antonović, D.G.; Jokić, B.M.; Zec, S.P.; Tanasković, S.T.; Raičević, S. Synthesis of fluorine substituted hydroxyapatite nanopowders and application of the central composite design for determination of its antimicrobial effects. *Appl. Surf. Sci.* **2014**, *290*, 346–352. [CrossRef]
21. Zhou, W.; Zhang, J.; Liu, Y.; Li, X.; Niu, X.; Song, Z.; Feng, S. Characterization of anti-adhesive self-assembled monolayer for nanoimprint lithography. *Appl. Surf. Sci.* **2008**, *255*, 2885–2889. [CrossRef]
22. Kraus, W.; Nolze, G. POWDER CELL—A program for the representation and manipulation of crystal structures and calculation of the resulting X-ray powder patterns. *J. Appl. Crystallogr.* **1996**, *29*, 301–303. [CrossRef]
23. Shannon, R.D. Revised effective ionic radii and systematic studies of interatomic distances in halides and chalcogenides. *Acta Crystallogr. Sect. A Cryst. Phys. Diffr. Theor. Gen. Crystallogr.* **1976**, *32*, 751–767. [CrossRef]
24. Ciobanu, C.S.; Iconaru, S.L.; Massuyeau, F.; Constantin, L.V.; Costescu, A.; Predoi, D. Synthesis, structure, and luminescent properties of europium-doped hydroxyapatite nanocrystalline powders. *J. Nanomater.* **2012**, *2012*, 942801. [CrossRef]
25. Ciobanu, C.S.; Popa, C.L.; Predoi, D. Cerium-doped hydroxyapatite nanoparticles synthesized by the co-precipitation method. *J. Serb. Chem. Soc.* **2016**, *81*, 433–446. [CrossRef]
26. Fleet, M.E.; Pan, Y. Site preference of rare earth elements in fluorapatite. *Am. Mineral.* **1995**, *80*, 329–335. [CrossRef]
27. Regnier, P.; Lasaga, A.C.; Berner, R.A.; Han, O.H.; Zilm, K.W. Mechanism of CO32—Substitution in carbonate-fluorapatite: Evidence from FTIR spectroscopy, 13C NMR, and quantum mechanical calculations. *Am. Mineral.* **1994**, *79*, 809–818.
28. Yoder, C.; Pasteris, J.; Worcester, K.; Schermerhorn, D.; Sternlieb, M.; Goldenberg, J.; Wilt, Z. Dehydration and rehydration of carbonated fluor-and hydroxylapatite. *Minerals* **2012**, *2*, 100–117. [CrossRef]
29. Gibson, I.R.; Bonfield, W. Novel synthesis and characterization of an AB-type carbonate-substituted hydroxyapatite. *J. Biomed. Mater. Res. Part A* **2002**, *59*, 697–708. [CrossRef]
30. Elliott, J.C. *Structure and Chemistry of the Apatites and Other Calcium Orthophosphates*; Elsevier: Amsterdam, The Netherlands, 1994.
31. Lafon, J.P.; Champion, E.; Bernache-Assollant, D.; Gibert, R.; Danna, A.M. Termal decomposition of carbonated calcium phosphate apatites. *J. Therm. Anal. Calorim.* **2003**, *72*, 1127–1134. [CrossRef]
32. Doat, A.; Pellé, F.; Gardant, N.; Lebugle, A. Synthesis of luminescent bioapatite nanoparticles for utilization as a biological probe. *J. Solid State Chem.* **2004**, *177*, 1179–1187. [CrossRef]
33. Sobierajska, P.; Pazik, R.; Zawisza, K.; Renaudin, G.; Nedelec, J.M.; Wiglusz, R.J. Effect of lithium substitution on the charge compensation, structural and luminescence properties of nanocrystalline Ca 10 (PO 4) 6 F 2 activated with Eu 3+ ions. *CrystEngComm* **2016**, *18*, 3447–3455. [CrossRef]
34. Sardar, D.K.; Russell, C.C., III. Optical transitions, absorption intensities, and intermanifold emission cross sections of Pr3+(4f2) in Ca5(PO4)3F crystal host. *J. Appl. Phys.* **2004**, *95*, 5334–5339. [CrossRef]

35. Gaft, M.; Reisfeld, R.; Panczer, G.; Shoval, S.; Garapon, C.; Boulon, G.; Strek, W. Luminescence of Eu (III), Pr (III) and Sm (III) in carbonate-fluor-apatite. *Acta Phys. Pol. Ser. A Gen. Phys.* **1996**, *90*, 267–274. [CrossRef]
36. Reisfeld, R. Spectra and energy transfer of rare earths in inorganic glasses. *Rare Earths* **1973**, *13*, 53–98. [CrossRef]
37. Ignjatović, N.L.; Mančić, L.; Vuković, M.; Stojanović, Z.; Nikolić, M.G.; Škapin, S.; Jovanović, S.; Veselinović, L.J.; Uskoković, V.; Lazić, S.; et al. Rare-earth (Gd3+, Yb3+/Tm3+, Eu3+) co-doped hydroxyapatite as magnetic, up-conversion and down-conversion materials for multimodal imaging. *Sci. Rep.* **2019**, *9*, 16305. [CrossRef] [PubMed]
38. Petkovšek, Z.; Eleršič, K.; Gubina, M.; Zgur-Bertok, D.; Starčič Erjavec, M. Virulence potential of Escherichia coli isolates from skin and soft tissue infections. *J. Clin. Microbiol.* **2009**, *47*, 1811–1817. [CrossRef]